Detailed microstructure analysis of as-deposited and etched porous ZnO films

Congcong Shang, Yohan Thimont, Antoine Barnabé, Lionel Presmanes, Isabelle Pasquet, Philippe Tailhades

Detailed microstructure analysis of as-deposited and etched porous ZnO films

Congcong Shang, Yohann Thimont, Antoine Barnabé*, Lionel Presmanes, Isabelle Pasquet, Philippe Tailhades

Université de Toulouse III Paul Sabatier, CIRIMAT–UMR CNRS 5085, Institut Carnot, 118 route de Narbonne, 31062 Toulouse Cedex 9, France

Keywords:
ZnO
Thin films
Surface morphology
Optical properties
TCO
Chemical etching

A B S T R A C T

ZnO nanostructured materials in thin film forms are of particular interest for photovoltaic or photocatalysis processes but they suffer from a lack of simple methods for optimizing their microstructure. We have demonstrated that microporous ZnO thin films with optimized inter grain accessibility can be produce by radio frequency magnetron sputtering process and chemical etching with 2.75 mM HCl solution for different duration. The as-deposited ZnO thin films were first characterized in terms of structure, grain size, inter grain space, open cavity depth and total thickness of the film by XRD, AFM, SEM, profilometry and optical measurements. A specific attention was dedicated to the determination of the surface enhancement factor (SEF) by using basic geometrical considerations and images treatments. In addition, the porous fraction and its distribution in the thickness have been estimated thanks to the optical simulation of the experimental UV–Visible–IR spectrums using the Bruggeman dielectric model and cross section SEM images analysis respectively. This study showed that the microstructure of the as-deposited films consists of a dense layer covered by a porous upper layer developing a SEF of 12–13 $m^2\,m^{-2}$. This two layers architecture is not modified by the etching process. The etching process only affects the upper porous layer in which the overall porosity and the inter-grain space increase with the etching duration. Column diameter and total film thickness decrease at the same time when the films are soaked in the HCl bath. The microporous structure obtained after the etching process could generate a great interest for the interfaces electronic exchanges for solar cells, photocatalysis and gas sensors applications.

1. Introduction

The wide bandgap semiconductors play an essential role in various electronic and opto-electronic applications being produced today [1,2]. In this class of Transparent Conducting Oxide (TCO) materials, nanostructured zinc oxide (ZnO) received a considerable attention over past few years because of its low cost, its high transparency associated with a high mobility of charge carriers and because it does not give rise to environmental concerns [3–6]. For photovoltaic applications such as thin films in Si-solar cells, ZnO can be used in TCO front contact [7] but also to provide additional optical functions like light scattering [8–10]. Nanostructured ZnO is also of particular interest for organic and dye sensitized solar cells [11,12] or photocatalysis process [13] because it can be nanostructured into nanowires and rods, which makes it ideal for infiltration of the absorption layer. ZnO nanostructured materials importance is manifested in many papers that have been issued for its synthesis using numerous soft chemistry pathways, chemical and physical deposition technologies [14–16]. Among them, sputtering technic is particularly used to deposit ZnO thin film materials because of its robustness, large-area and high rates manufacturing capabilities [**3,6,7,10,17**].

Other favorable aspects of ZnO include its chemical reactivity to many acids leading to many opportunities for wet chemical etching. Many etching methods using HCl have been reported to develop a rough surface and then induce a light scattering effect, which can significantly improve light trapping (and therefore current photogeneration) [8,9,18–21]. HCl etching agent was also used to study the corrosion behavior of ZnO thin films in acid solutions [22].

In this study, we report a novel approach to the fabrication of sub-micrometric porous ZnO thin films. First, ZnO thin films are deposited by Radio Frequency (RF) cathodic magnetron sputtering. Deposition parameters are adjusted to maximize the inter-granular porosity in the as-deposited ZnO films. The nanostructure of these

* Corresponding author. Tel.: +33 561557751; fax: +33 561556163.
E-mail address: barnabe@chimie.ups-tlse.fr (A. Barnabé).

films is then controlled using wet chemical etching in weakly concentrated HCl media. However, unlike the usually obtained micrometric pit by HCl etching for light scattering property [8,9], we present a new consequence of the etching effect at the nanometric scale, for the modification of accessibility of the surface to gases and liquids. A detailed characterization, including XRD, SEM, AFM, optical analysis, optical simulation, of both structure and microstructure of ZnO thin films before and after etching, is presented. Furthermore, two calculations methods are evaluated for the estimation of the surface enhancement factor (SEF).

2. Material and methods

2.1. Deposition of ZnO thin films

Thin films were deposited in an Alcatel CIT, type A450, conventional planar system, using a commercial ceramic ZnO target (Neyco, purity 99.99%). The studied samples were deposited onto glass substrates with $1.3 \times 2.6\,cm^2$ in dimension carried by water cooled substrate holder. The RF power was set as 50 W with magnetron, and argon was used as deposition gas.

Many authors reported that the microstructure of the thin films prepared by sputtering can be tuned by changing deposition conditions [23,24]. This has been confirmed by the microstructure study of spinel oxide thin films ($Zn_{0.87}Fe_{2.13}O_4$ [25] and $CoMnFeO_4$ [26,27]) deposited using the same RF sputtering apparatus by changing the deposition gas pressure (P_{Ar}) and substrate to target distance (D_{ST}). With the increase of P_{Ar} and D_{ST}, particles with short mean free path are produced. Such deposition conditions give rise to particles with low energy and large incidence angle, i.e. with low mobility of ad-atoms and high shadowing effect for the growth of thin films. Therefore, the highest $P_{Ar} = 2$ Pa and $D_{ST} = 8$ cm values allowed by the deposition system were used in an attempt to prepare ZnO thin films with porous microstructure and large accessible surface.

Under these conditions, the bombardment of the target is very intense especially on the erosion ring due to the concentrated plasma caused by magnetron. The chemical reduction of the target surface tends to increase progressively each time plasma is switched on. To prevent this phenomenon and to avoid high oxygen deficiency and heterogeneity in the deposited thin films, oxygen (1% of O_2 in Ar) was systematically introduced in the pre-sputtering gas during 20 min prior to each deposition (under pure Ar).

A deposition rate close to 8 nm/min was determined from set of reference samples deposited in the 10–90 min duration range.

2.2. Wet chemical etching of ZnO thin films

A simple experimental set-up was used for all the etching tests. In a polymer container equipped with a tight cap, 50 ml water solution of HCl (2.75 mM) was prepared first. During each etching, the whole piece of sample was immersed into the solution. Once the etching was finished, the sample was rinsed immediately by de-ionized water, and rinsed for several times, using an ultrasound bath of de-ionized water. Finally, the sample was dried using compressed nitrogen gas flow. All these experiments were done at room temperature. Five different samples were submitted to HCl bath for durations ranging from 10 to 60 min.

2.3. Characterization techniques

The thin film thickness was measured by both mechanical profilometry ($t_{profilo}$) using a Dektak 3030ST apparatus and optical transmittance ($t_{optical}$) according to the interferometric method [28]. The crystalline structure of thin films was studied using Bruker AXS D4 Endeavor diffractometer, equipped with a 1D LynxEye detector. The diffraction patterns were recorded in θ–2θ mode from 20 to 100° with a step size of 0.016° and a counting time of 0.13 s for each step. Copper anode is used as X-ray source, with the corresponding Kα radiation ($\lambda_{K\alpha1} = 1.5405$ Å, $\lambda_{K\alpha2} = 1.5443$ Å). Nickel filter was used to eliminate the K_β ray and fluorescence. Atomic Force Microscope (AFM) analyses of the thin films were performed using a nanoscope III Dimension 3000 Veeco Digital Instrument (tapping mode) with super sharp tips for the study of surface morphology. A JEOL JEM 6700F field emission gun Scanning Electron Microscope (SEM) was also engaged in the surface morphology analysis, as well as the morphology of the cross-section. Optical properties of the thin films, notably the transmittance and reflectance, were analyzed by a Bentham PVE 300 photovoltaic characterization system, with integrating sphere operation mode.

2.4. Image analysis treatment for SEF calculation

The Surface Enhanced Factor (SEF) is the surface on which molecules can be adsorbed for a film per unit area. SEF is simply defined as the ratio of the real to the projected geometric surface.

In the model developed for $CoMnFeO_4$ thin films by Oudrhiri-Hassani et al. [27], the microstructure of a thin sputter-deposited film is simply described by cylindrical grain shape with hemispherical domes. Near the substrate, the interface is considered as dense layer according to the model of Czigany et al. [29]. A simple scheme of this model is represented in Fig. 1a. In this model, SEF represents the sum of the normalized area of the bottom of the interstices between the columns (S_{Cavity}), the lateral surface area of the columns (S_{Wall}) and the surface area of the domes (S_{Dome}). SEF is calculated by geometrical consideration using the thickness of the porous layer (t_{PL} entitled L_3 in the original paper) and the mean diameter of the columns (d) estimated from SEM micrographs in cross-section and planar views, according to Eq. (1):

$$SEF = \frac{(4t_{PL} + d)\pi + 2d\sqrt{3}}{2d\sqrt{3}} \quad (1)$$

In this work, the Gwyddion software [30] was used to treat and analyze SEM surface view of the ZnO thin film in order to more finely estimate the SEF through a better estimation of the area of the bottom of the interstices between the columns and the lateral surface area of the columns. After a normalization of the gray scale, a mathematical segmentation treatment was applied and followed by a borderkill operation to obtain an equivalent threshold mask of the image (Fig. 1b). Threshold has been fixed at 64% of the maximum of the normalized grey scale. This value was arbitrarily set in order to reveal a maximum of inter-granular areas (area of the bottom of the interstices between the columns) without adding wrong grain boundaries inside the grains. After the inversion of the mask, marked patterns have been used for the localization, quotation and the size characterization of the open cavities (as the perimeter and the projected surface area) (Fig. 1c). The total perimeter (P_t) has been deduced from the sum of the perimeter of each marked open cavities. Here we supposed that the unmarked zones represented in black in Fig. 1c consist of grains only. The grains have also been modelled as pseudo-cylinders with hemispherical domes at the surface of the film. As for the previous model, SEF is the sum of S_{Cavity}, S_{Wall} and S_{Dome}. The area of the bottom of the interstices between the columns, i.e. the surface of the whole projected open cavities is determined directly by the threshold operation (S_{Cavity}). The lateral surface area of the columns (S_{Wall}), i.e. the internal surface wall of the open cavities can be calculated by multiplying the total perimeter of the open cavities P_t by the thickness of the porous layer t_{PL}. The relation between the dome surface (S_{Dome}) and the grain projected surface ($S_{Projected\ Total} - S_{Cavity}$) is mathematically equal to 2: the dome surface is equal to $2\pi r^2$, i.e. half of the surface area of a sphere of radius r and the grain projected surface is equal to πr^2, i.e.

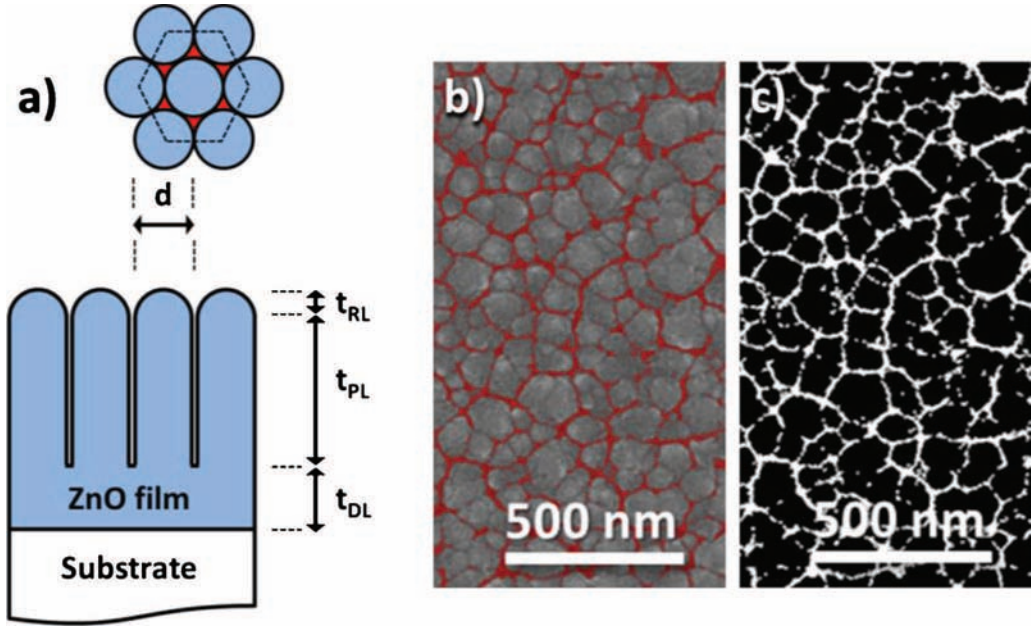

Fig. 1. (a) Simplified microstructure of the as deposited ZnO thin film used for the estimation of Surface Enhancement Factor (SEF) whereas d is the average column diameter and t_{RL}, t_{PL}, t_{DL} the thicknesses of the Roughness Layer, Porous Layer and Dense Layer respectively. The total thickness of the film is $t = t_{RL} + t_{PL} + t_{DL}$. (b) calculated mask (in red) superposed to the original image SEM micrograph obtained after the threshold operation and (c) extracted mask used for the calculation of the total perimeter of open cavities (P_t).

the area of a disk of the same radius r. As a result, from t_{PL} estimated from the SEM micrograph, and P_t and S_{Cavity} obtained by the image treatment, SEF can be calculated according to Eq. (2):

$$SEF = \frac{S_{Cavity} + t_{PL} \cdot P_t + 2(S_{Projected\,Total} - S_{Cavity})}{S_{Projected\,Total}} \quad (2)$$

3. Results and discussion

3.1. As-deposited ZnO thin films

XRD measurement indicates that the as-deposited ZnO films are polycrystalline with the hexagonal wurtzite structure. A high c-axis orientation perpendicular to the substrate is observed in contrast to the target used for deposition. An example of the XRD pattern of the thin film is shown in Fig. 2. The lattice parameters $a = 3.29(1)$ Å and $c = 5.183(7)$ Å for these thin films were deduced from the (0 0 2) and (1 0 3) peaks respectively located at 34.586° and 62.875° in 2θ. They are very close to the theoretical values of $a = 3.2498$ Å and $c = 5.2066$ Å respectively (JCPDS card No. 36-1451).

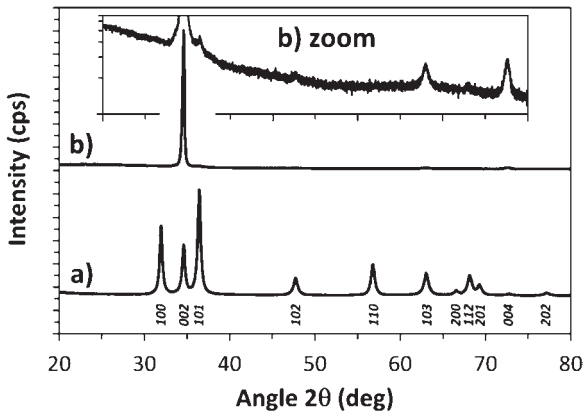

Fig. 2. X-Ray diffraction patterns of (a) ZnO powder and (b) 600 nm-thick ZnO as-deposited thin film.

The microstructure of the as-deposited thin films was studied by both AFM and SEM (in surface and cross-section views). A relatively flat surface was obtained for these thin films with a RMS roughness of 13 nm measured by AFM (Fig. 3a). From the SEM surface view (Fig. 3b), an average particle size of approximately 110 nm was measured and narrow inter-grain spaces were evidenced. The cross-sectional SEM image (Fig. 3c) showed columnar-type microstructure with inverted conical-shaped. These grains grow perpendicular to the glass substrate and are confined in a bi-layer configuration as previously described by C. Besleaga et al. [31]. From the substrate to the surface, a Compact Layer (CL) with small grain size first appears with an average thickness of 200 nm followed by a 400 nm thick Porous Layer (PL) with better defined larger grains. The upper porous layer is due to the shadow effect of the initially developed columns. This bi-layer configuration can usually be seen for such relatively thick sample due to the evolution of wavy interface as previously reported by Czigany et al. [29] and simulated by mathematical models. For lower thicknesses, the wavy surface of the thin film throughout the growing direction has no significant evolution: the shadow effect does not occur and the film formed is compact.

The SEF, which is simply defined as the ratio of the real to the projected geometric surface, is a parameter that can be used for porous thin film evaluation. For the SEF determination, BET measurement on thin films is then very efficient but requires a large quantity of deposits which makes it time consuming and not so easy to use. An easier approach is given by the determination of SEF using a simple geometrical model in which characteristic parameters are supplied by microstructural observations. Indeed we demonstrated previously that SEF can be well estimated by using the thickness of the porous layer and the mean grain size [27]. Thus in our current work, this method based on a mathematical model has been used to estimate SEF value (Eq. (1)). From the SEM observations of the $t = 600$ nm thick ZnO film (Fig. 3b and c Fig. 3), the dense layer thickness has been approximated to 1/3 of the total thickness ($t_{DL} = 200$ nm) and the column average diameter estimated to $d = 110$ nm. With a thickness of the roughness layer estimated to $d/2$ ($t_{RL} = 55$ nm), the thickness of the porous layer was

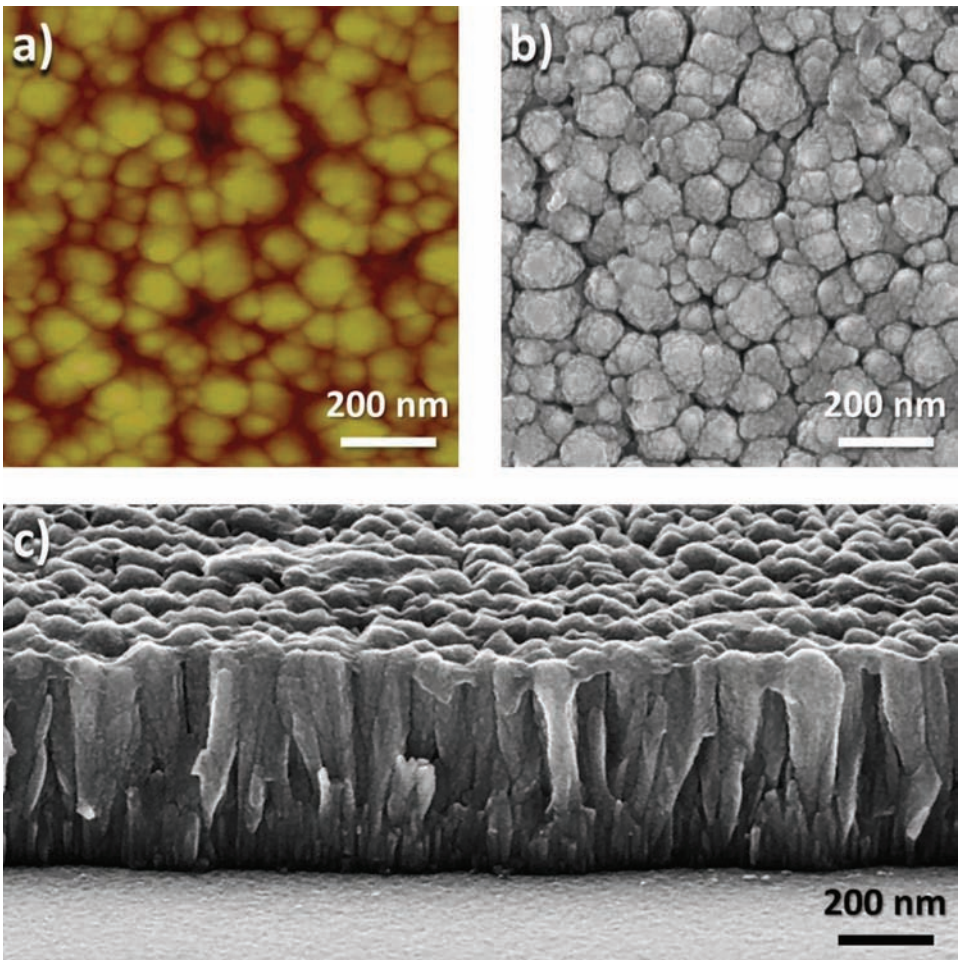

Fig. 3. (a) AFM and (b) SEM surface views and (c) SEM tilted cross section view of as-deposited 600 nm thick ZnO film.

deduced ($t_{PL} = t - t_{RL} - t_{DL} = 345$ nm). Finally the whole microstructure of the film can be modeled and the SEF can then be estimated to be 13.3 $m^2\ m^{-2}$ using this model.

Using the SEM surface view (Fig. 3b), a total perimeter P_t of 30.2 μm and a surface of the whole projected open cavities S_{Cavity} of 0.126 μm^2 have been determined by image treatment realized on a total projected surface $S_{Projected\ Total}$ of 1 μm^2. With identical thickness of the porous layer ($t_{PL} = 345$ nm), the SEF is then estimated to be 12.3 $m^2\ m^{-2}$ by application of Eq. (2). This is in good accordance with the result obtained previously and then validates the simple microstructural model represented in Fig. 1a.

Finally the microstructure of 600 nm thick as-deposited ZnO thin films can be summarized as follow. A dense under layer accounting for about 1/3 of the total thickness, i.e. about 200 nm, and a porous upper layer (~350 nm thick) surrounded by a roughness layer corresponding to the surface waviness of the film (~50 nm thick) which both occupies the remaining about 2/3 of the total thickness. From this geometrical consideration and by using a simple geometrical model, the surface enhancement factor (SEF) has been estimated to be worth close to 12–13 $m^2\ m^{-2}$. Even though the deposition condition was adjusted to produce a highly porous microstructure (high argon pressure and large substrate-to-target distance), the as-deposited ZnO thin film develop much less accessible surface compared to spinel $CoMnFeO_4$ thin films [27] prepared under similar deposition conditions. This result is mainly explained by the larger column diameters and higher deposition rates which are obtained in the zinc oxide layer. It can be due to the simple chemical composition of ZnO that allows an easier crystallization than more complex oxide like the cobalt-manganese spinel ferrite composed of three cations and two cationic sublattices.

3.2. HCl-etched ZnO thin films

The oriented microstructure of the as deposited ZnO thin films allows generating attractive SEF values but with limited inter-grain space for gas sensor and dye sensitized solar cells applications. Chemical etching with acid solution can generate anisotropic effects [21,32,33] and then increases the inter-grain space without notable microstructural modification. This anisotropic effect can be modulated by the use of various etching method, agent and conditions. For instance, a dominant vertical etching process has been obtained on rf-sputtered ZnO film etched electrochemically using 10 wt% KOH solution [34,35]. In this work, post-chemical etching was then performed in a second step in order to enlarge the inter-grain space and increase the accessibility of the thin film surface area. A serie of 600 nm thick ZnO thin films were etched in 2.75 mM HCl water solution for different duration. The thin films characteristics were then evaluated according to etching duration.

The optical characteristics (total transmittance TT, total reflectance TR and deduced total absorbance TA) of the as-deposited and etched ZnO thin films for various etching times are plotted in Fig. 4.

The as-deposited and etched thin film thicknesses were measured by both mechanical profilometry ($t_{profilo}$) and optical transmittance ($t_{optical}$). Results are reported in the Table 1 within the average total transmittance ($TT_{400\text{-}800}$) in the visible light range

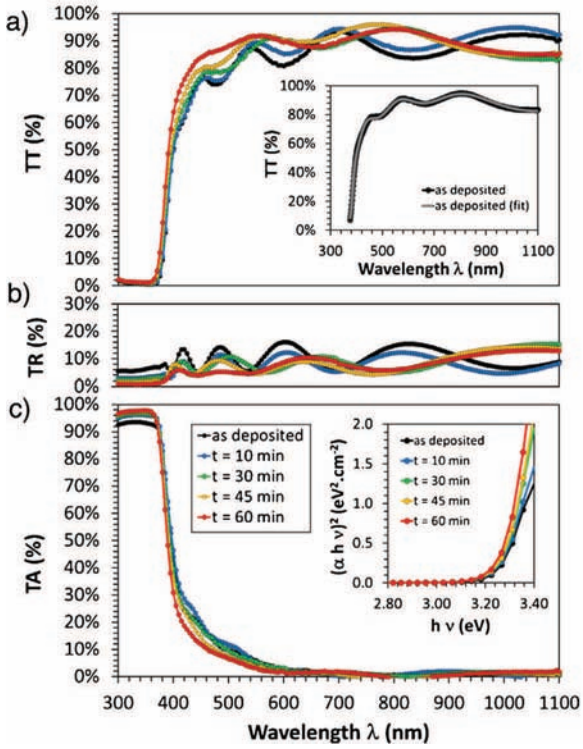

Fig. 4. Optical spectra of ZnO thin films as a function of the etching duration *t*. (a) Total Transmittance TT. Inset shows the experimental and simulated TT spectra of as-deposited film. (b) Total Reflectance TR. (c) Total absorbance TA. Inset shows the Tauc plot for estimation of direct allowed optical gap.

$(400 < \lambda < 800\,\text{nm})$ extracted from TT measurements represented in Fig. 4a. Haze parameter defined as the ratio of diffused to total transmitted light is also reported as soon as diffused transmitted light is measurable. Accuracies estimated by reproducibility and repeatability tests are less than 3% for all the reported values in the Table 1.

Table 1
Characteristic values from different analyses of HCl etched samples for different etching duration.

Etching duration (min)	0	10	20	30	45	60
$t_{profilo}$ (nm)	610	558	491	428	365	–
$t_{optical}$ (nm)	620	547	506	420	401	–
$TT_{400-800}$ (%)	83	84	85	85	88	88
Haze (%)	–	–	–	2.7	2.4	2.4

A clear decrease of thicknesses ($t_{profilo}$ and $t_{optical}$) was observed with the increase of etching duration for the first 45 min of etching. For longer etching duration (60 min), the estimation of thicknesses from both profilometry and optical measurements became very difficult and leads to limited accuracy due to the less defined step and interferences on transmittance spectra respectively. An average vertical etching rate of $5.6\,\text{nm}\,\text{min}^{-1}$ is deduced for etching duration smaller than 45 min.

The average transmittance in visible range and the total transmittance in absorption range both increased with the increase of etching duration, which is in accordance with the decrease of thin film thickness. The absorption edge is unaffected by the etching treatment (Eg = 3.24 eV) as shown by the Tauc plot [36] in the insert of the Fig. 4c. For 30 min of etching duration and more, the diffused transmitted light starts to be measurable and few percent (2.4–2.7%) could be calculated for the haze factor (Table 1) due to the increase of surface roughness and light scattering.

TT and TR spectra of the as-deposited film were also simulated with the SCOUT software [37] using a Drude model coupled with an interband Kim oscillator [38]. During simulation, the total thickness of the thin films was divided into two layers (a top porous layer stacked on a dense layer) according to the previous microstructural characterizations (Fig. 3c) and modelization (Fig. 1a). It can be also noticed that the estimation of the volume fraction of the ZnO top layer was obtained by the Bruggeman dielectric model [39]. By refinement of different parameters, including the top porous layer volume fraction ($PL\%^{Vol}$) and thickness (t_{PL}) and the under

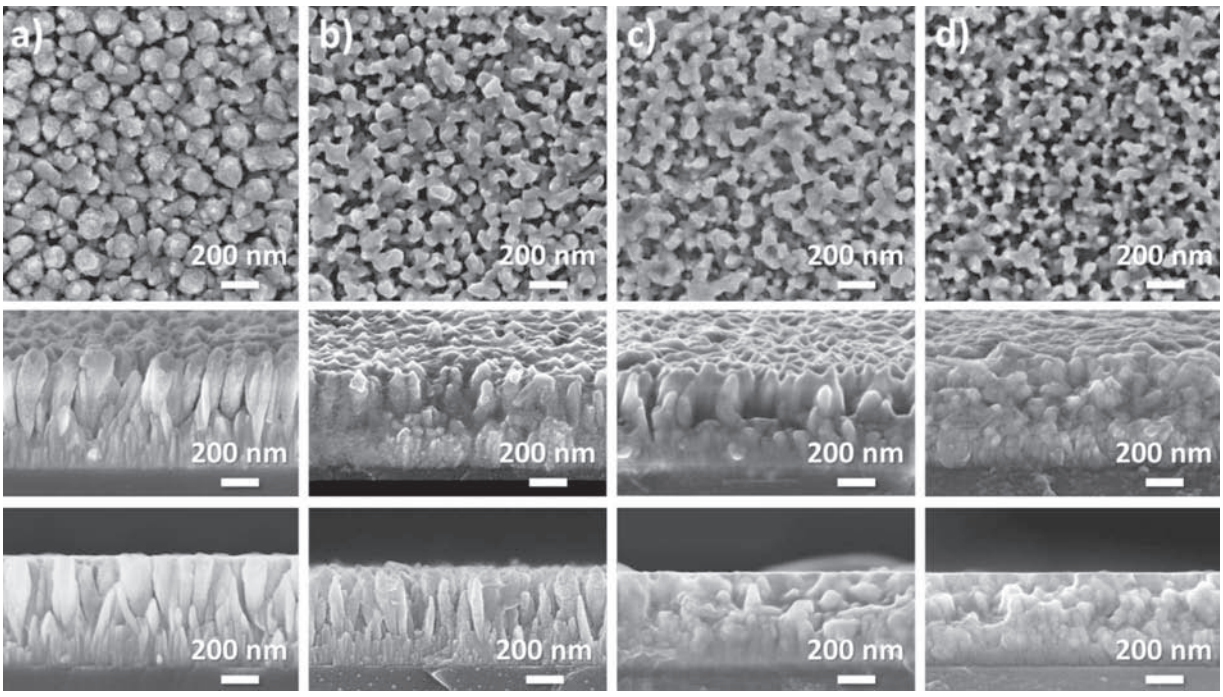

Fig. 5. Surface, tilted and perpendicular views of HCl etched ZnO thin films for (a) 10 min, (b) 30 min, (c) 45 min and (d) 60 min duration.

dense layers thickness (t_{DL}), the simulated spectra were fitted to the experimental data. The optimal fit of the experimental as-deposited total transmittance spectrum (insert Fig. 4a) is obtained with $PL\%^{Vol} = 93\%$, $t_{PL} = 458$ nm and $t_{DL} = 130$ nm. These parameters are in good agreement with the previous SEM characterization.

To estimate the evolution of the porous fraction with the etching duration, the evolution of the microstructure of the ZnO films after 10, 30, 45 and 60 min etching duration was then investigated by SEM analysis. The results are presented in Fig. 5. The corresponding image of the as-deposited sample was previously shown in Fig. 3. Upon etching duration, the SEM micrographs in cross-section views (Fig. 3c and Fig. 5) showed a reduction of the thickness of the top porous layer (t_{PL}) associated with a decrease of its volume fraction, i.e. and increase of its porosity. However, the under dense layer thickness (t_{DL}) variation has no clear trend at different etching duration. According to the surface views (Fig. 3b and Fig. 5) and with the increase of etching duration, the grain size decreases significantly whereas the inter-grain space increases significantly. Therefore, considering the thickness diminution showed previously with the increase of etching duration, HCl acted both on the top of the grains and on the sides of the columns of the porous upper layer which are exposed to the etching solution through the inter-columnar pores previously highlighted. From the cross-sectional views (Fig. 5), it appears that the bi-layer microstructure observed in as-deposited thin film (Fig. 3b) has been preserved. After 10 min of etching, the grains of porous layer showed less compact microstructure compared to the as-deposited thin films. The inter-grain space slightly increased for the entire porous layer. When the etching duration increased to 30 min, the grain size appears to be much smaller than that of as-deposited and 10 min etched thin films. However, for 60 min etching, the porous layer was heavily attacked. In the meantime, the dense layer appears to be the same for the three samples. With 10 min of etching, the etching effect already reached the interface of the two layers, however with 50 min more, the dense layer remains roughly the same. The different microstructures observed in upper and under layers lead then to etching rates which differs strongly for the column located in the porous layer and the dense layer placed in the deeper part of the ZnO film and thus less accessible. The schematic microstructure of a ZnO thin film can be seen in the Fig. 6a at initial and final stage of the partial etching process.

The average inter-grain space was estimated using the same SEM images treatment used for the as-deposited analysis. These values represent the average size of the marked zones (Fig. 6b). The inter-grain space (d_{IGS}) distributions at different etching duration were also investigated using the surface treatment analysis which allows determining the distribution of the maximum radius of the inscribed circle in the marked zone of the mask and has been reported in the insert of Fig. 6b. From this distribution, the percentage of d_{IGS} expressed in cumulative past (%) versus the size was used to determine the median value ($d_{50\%} = d_{IGS}$) and the error bars ($d_{45\%}$ and $d_{55\%}$). For the as-deposited thin films, the d_{IGS} distribution is quite narrow with a maximum occurrence near 30 nm. With the increase of etching duration to 60 min, the d_{IGS} distribution became broader and the maximum is slightly shifted to higher values ($d_{IGS} \approx 60$ nm for 60 min). These results confirmed again the increase in average inter-grain space, and furthermore, the broadening of distribution suggests the non-homogenous etching in depth throughout the whole thin film layer.

During the etching, both the top porous layers including the roughness layer ($t_{PL} + t_{RL}$) and the bottom dense layer (t_{DL}) decrease (Fig. 6c). However, according to the slightest accessibility of the dense under layer, the vertical etching rate (from the surface of the film to the film-substrate interface) of the porous layer is more important. The evolution of the SEF calculated by SEM image analysis as a function of the etching duration is reported in the Fig. 6d. The Surface Enhancement Factor decreases from 12.3 $m^2\,m^{-2}$ to 7.2 $m^2\,{}^{-}m^2$ with the etching duration due to both the decrease in thickness of the top porous layer and the decrease of the mean column diameter. Finely, the increase of inter-grain space promotes the accessibility of molecules within the film, which could reveal a high potential for example for applications such as gas sensing (improvement of sensibility and response time) or Gräetzel cells (absorbing dye inside the porosity).

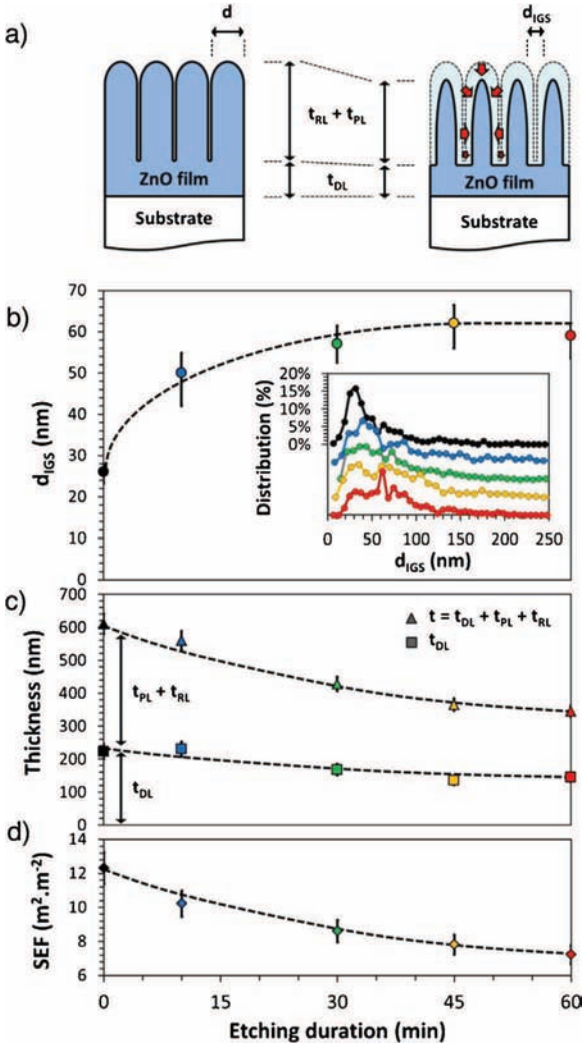

Fig. 6. (a) Schematic representation of the microstructure of a ZnO thin film as deposited and after partial etching in HCl solution. (b) Average inter grain space (d_{IGS}) and its distribution determined from the maximum radius of the inscribed circle in the marked zones (insert), (c) thickness of the layers (total thickness t and dense layer thickness t_{DL}) and (d) the SEF for different etching durations. The dotted curves are placed to guide viewer.

4. Conclusion

Highly *c*-oriented hexagonal wurtzite ZnO thin films have been prepared by radio-frequency cathodic magnetron sputtering under an argon pressure of 2 Pa and a target-to-substrate distance of 8 cm. The as-deposited films are made of a dense under layer accounting for 1/3 of the film, surrounded by a porous microstructure for the remaining part. A surface enhancement factor (SEF) close to 12–13 $m^2\,m^{-2}$ has been determined by two calculation methods. Thin films were etched by low concentration HCl solution then analyzed by profilometry, BET, SEM, AFM and UV–Vis–IR spectrophotometer. By applying SEM image treatment method, mathematical model and optical simulations, the thicknesses of the

dense and porous parts of the film, and the inter-grain space were studied in detail. The etched films show a similar microstructure to that of the as deposited thin film, with a porous layer stacked on dense layer. The top porous layer thickness decreases with the etching duration in opposition with the thickness of the dense layer remaining constant. Globally, a significant decrease of the total thin film thickness and the enlargement of the inter-grain space throughout the entire porous layer were observed with the increase in HCl etching duration. Accordingly, HCl etching performed both along (top of the columns) and perpendicular (side of the columns) to *c*-axis with a lower etching rate at grain boundaries which generated an increase of the porosity of the porous upper layer in nanometer scale.

Finally, even with partial loss of thickness, the HCl etching can still be very interesting for increasing the accessibility for gas and molecules within ZnO thin films. The microstructural characteristics of the etched ZnO thin films are very interesting for the electronic exchange as, for instance, in solar cells, gas sensors and photo catalysts applications. Moreover, the wet etching at nanometer scale of a film deposited under optimized sputtering conditions with a well-controlled porous microstructure can be applied to any other thin film composition.

References

[1] P. Barquinha, R. Martins, L. Pereira, E. Fortunato, Transparent Oxide Electronics: From Materials to Devices, Wiley, 2012, 978-0-470-68373-6.
[2] D.S. Ginley, C. Bright, Transparent and conducting oxides, MRS Bull. 25 (8) (2000) 15–21.
[3] T. Minami, T. Yamamoto, T. Miyata, Highly transparent and conductive rare earth-doped ZnO thin films prepared by magnetron sputtering, Thin Solid Films 366 (2000) 63–68.
[4] Ü. Özgür, D. Hofstetter, H. Morkoç, ZnO devices and applications: a review of current status and future prospects, Proc. IEEE 98 (2010) 1255–1268.
[5] Ü. Özgür, Y.I. Alivov, C. Liu, A. Teke, M.A. Reshchikov, S. Doğan, V. Avrutin, S.J. Cho, H. Morkoç, A comprehensive review of ZnO materials and devices, J. Appl. Phys. 98 (2005), 041301-1–103.
[6] K. Ellmer, A. Klein, B. Rech, Transparent Conductive Zinc Oxide: Basics and Applications in Thin Film Solar Cells, Springer, 2008, ISBN 978-3-540-73612-7.
[7] E. Fortunato, D. Ginley, H. Hosono, D. Paine, Transparent conducting oxides for photovoltaics, Mater. Res. Soc. Bull. 32 (2007) 242–247.
[8] K.C. Lai, F.J. Tsai, J.H. Wang, C.H. Yeh, M.P. Houng, Wet-etch texturing of ZnO:Ga back layer on superstrate-type microcrystalline silicon solar cells, Sol. Energy Mater. Sol. Cells 95 (2011) 1583–1586.
[9] J. Hüpkes, H. Zhu, J.I. Owen, G. Jost, E. Bunte, Instabilities in reactive sputtering of ZnO:Al and reliable texture-etching solution for light trapping in silicon thin film solar cells, Thin Solid Films 520 (2012) 1913–1917.
[10] M. Berginski, J. Huepkes, W. Reetz, B. Rech, M. Wuttig, Recent development on surface-textured ZnO:Al films prepared by sputtering for thin-film solar cell application, Thin Solid Films 516 (2008) 5836–5841.
[11] L. Bahadur, S. Kushwaha, Highly efficient nanocrystalline ZnO thin films prepared by a novel method and their application in dye-sensitized solar cells, Appl. Phys. A 109 (2012) 655–663.
[12] G. Jimenez-Cadena, E. Comini, M. Ferroni, A. Vomiero, G. Sberveglieri, Synthesis of different ZnO nanostructures by modified PVD process and potential use for dye-sensitized solar cells, Mater. Chem. Phys. 124 (2010) 694–698.
[13] Y. Sivalingam, E. Martinelli, A. Catini, G. Magna, G. Pomarico, F. Basoli, R. Paolesse, C. Di Natale, Gas-sensitive photoconductivity of porphyrin-functionalized ZnO nanorods, J. Phys. Chem. C 116 (2012) 9151–9157.
[14] Z. Fan, J.G. Lu, Zinc oxide nanostructures: synthesis and properties, J. Nanosci. Nanotechnol. 5 (10) (2005) 1561–1573.
[15] L. Vayssieres, An aqueous solution approach to advanced metal oxide arrays on substrates, Appl. Phys. A 89 (2007) 1–8.
[16] C. Shang, A. Barnabé, Structural study and phase transition investigation in a simple synthesis of porous architected-ZnO nanopowder, Mater. Charact. 86 (2013) 206–211.
[17] M. Lalanne, J. Soon, A. Barnabé, L. Presmanes, I. Pasquet, P. Tailhades, Preparation and characterization of the defect–conductivity relationship of Ga-doped ZnO thin films deposited by nonreactive radio-frequency–magnetron sputtering, J. Mater. Res. 25 (2010) 2407–2414.
[18] S.H. Lee, B.H. Seo, J.H. Seo, Wet etching of gallium indium zinc oxide (GIZO) semiconductor for thin film transistor application, J. Korean Phys. Soc. 53 (5) (2008) 2603–2606.
[19] H. Zhu, J. Hüpkes, E. Bunte, J. Owen, S.M. Huang, Novel etching method on high rate ZnO:Al thin films reactively sputtered from dual tube metallic targets for silicon-based solar cells, Sol. Energy Mater. Sol. Cells 95 (2011) 964–968.
[20] X. Liao, X. Zhang, Zinc oxide nanostructures and their core-shell luminescence properties, J. Phys. Chem. C 111 (2007) 9081–9085.
[21] X.G. Han, Y.Q. Jiang, S.F. Xie, Q. Kuang, X. Zhou, D.P. Cai, Z.X. Xie, L.S. Zheng, Control of the surface of ZnO nanostructures by selective wet-chemical etching, J. Phys. Chem. C 114 (2010) 10114–10118.
[22] B.H. Seo, S.H. Lee, J.H. Seo, J.H. Jeon, H. Choe, Study on the wet etch behavior of a zinc-oxide semiconductor in acid solutions, J. Korean Phys. Soc. 53 (2008) 402–405.
[23] J.A. Thornton, The microstructure of sputter-deposited coatings, J. Vac. Sci. Technol. A 4 (1986) 3059–3065.
[24] A. Anders, A structure zone diagram including plasma-based deposition and ion etching, Thin Solid Films 518 (2010) 4087–4090.
[25] S. Capdeville, P. Alphonse, C. Bonningue, L. Presmanes, Ph. Tailhades, Microstructure and electrical properties of sputter deposited $Zn_{0.87}Fe_{2.13}O_4$ thin layers, J. Appl. Phys. 96 (2004) 6142–6146.
[26] I. Sandu, L. Presmanes, P. Alphonse, P. Tailhades, Nanostructured cobalt manganese ferrite thin films for gas sensor application, Thin solid Films 495 (2006) 130–133.
[27] F. Oudrhiri-Hassani, L. Presmanes, A. Barnabé, P. Tailhades, Microstructure, porosity and roughness of RF sputtered oxide thin films: Characterization and modelization, Appl. Surf. Sci. 254 (2008) 5796–5802.
[28] R. Swanepoel, Determination of the thickness and optical constants of amorphous silicon, J. Phys. E 16 (1983) 1214–1222.
[29] Z. Czigany, G. Radnoczi, Columnar growth structure and evolution of wavy interface morphology in amorphous and polycrystalline multilayered thin films, Thin Solid Films 347 (1999) 133–145.
[30] D. Necas and P. Klapetek, http://www.gwyddion.net/ Gwyddion software.
[31] C. Besleaga, G.E. Stan, A.C. Galca, L. Ion, S. Antohe, Double layer structure of ZnO thin films deposited by RF-magnetron sputtering on glass substrate, Appl. Surf. Sci. 258 (2012) 8819–8824.
[32] J. Elias, R. Tena-Zaera, G.Y. Wang, C. Lévy-Clément, Conversion of ZnO nanowires into nanotubes with tailored dimensions, Chem. Mater. 20 (2008) 6633–6637.
[33] H.Q. Wang, G.H. Li, L.C. Jia, G.Z. Wang, L. Li, General in situ chemical etching synthesis of ZnO nanotips array, Appl. Phys. Lett. 93 (2008), 153110-1–3.
[34] C.C. Ching, P.K. Ooi, S.S. Ng, M.A. Ahmad, Z. Hassan, H. Abu Hassan, M.J. Abdullah, Fabrication of porous ZnO via electrochemical etching using 10 wt% potassium hydroxide solution, Mater. Sci. Semicond. Process. 16 (2013) 70–76.
[35] C.C. Ching, S. Lee, P.K. Ooi, S.S. Ng, Z. Hassan, H. Abu Hassan, M. Abdullah, Optical and structural properties of porous zinc oxide fabricated via electrochemical etching method, Mater. Sci. Eng.B 178 (2013) 956–959.
[36] J. Tauc, R. Grigorovici, A. Vancu, Optical properties and electronic structure of amorphous germanium., Phys. Status Solidi 15 (1966) 627.
[37] W. Theiss, http://www.wtheiss.com/ CODE - A thin film analysis and design software.
[38] C.C. Kim, J.W. Garland, H. Abad, P.M. Raccah, Modeling the optical dielectric function of semiconductor: extension of the critical point parabolic band approximation, Phys. Rev. B Condens. Matter 45 (1992) 11749–11767.
[39] A.A.G. Bruggeman, Berechnung verschiedner physikalischer Konstanten von heterogenen Systemen, Annalen der Physik 24 (1935) 636–679.